Scalar flux modelling in turbulent flames using iterative deconvolution.

Z.M. Nikolaou,[*] R.S. Cant,[†] and L. Vervisch[‡]

(Dated: April 4, 2018)

Abstract

In the context of Large Eddy Simulations, deconvolution is an attractive alternative for modelling the un-closed terms appearing in the filtered governing equations. Such methods have been used in a number of studies for non-reacting and incompressible flows, however their application in reacting flows is limited in comparison. Deconvolution methods originate from clearly defined operations, and in theory can be used in order to model any un-closed term in the filtered equations including the scalar flux. In this study, an iterative deconvolution algorithm is used in order to provide a closure for the scalar flux term in a turbulent premixed flame by explicitly filtering the deconvoluted fields. The assessment of the method is conducted a priori using a three-dimensional direct numerical simulation database of a turbulent freely-propagating premixed flame in a canonical configuration. In contrast to most classical a priori studies, the assessment is more stringent as it is performed on a much coarser LES mesh which is constructed using the filtered fields as obtained from the direct simulations. For the conditions tested in this study, deconvolution is found to provide good estimates both of the scalar flux and of its divergence.

[*] Affiliation: University of Strathclyde. Current address: Computation-based Science and Technology Research Centre (CaSToRC), The Cyprus Institute, Nicosia, 2121, Cyprus; z.nicolaou@cyi.ac.cy

[†] Department of Engineering, University of Cambridge; rsc10@eng.cam.ac.uk

[‡] CORIA - CNRS, Normandie Université, INSA de Rouen Normandie, France; vervisch@coria.fr

I. INTRODUCTION

The numerical simulation of turbulent and reacting flows using Large Eddy Simulation (LES) is becoming ever more common in industry. This includes devices of realistic size and geometry in many different combustion and flow configurations [1, 2]. LES reduces the computational workload as compared to Direct Numerical Simulations (DNS) by filtering the governing equations using a spatial filter. The filtering process produces a smoothed version of the original field which can be resolved on a much coarser mesh [3]. The filtering operation however results in many un-closed terms in the governing equations, and accurate combustion and turbulence Sub-Grid Scale (SGS) models are required in order to close these terms [3]. Un-closed terms include filtered source terms, diffusion terms, scalar-flux terms, to name but a few. Scalar flux terms in particular, appear very often in many reacting LES formulations. These are given by,

$$f_{ia} = \bar{\rho} \left(\widetilde{u_i a} - \tilde{u}_i \tilde{a} \right) \tag{1}$$

where the overbar denotes a spatial filtering operation, and ˜ denotes a Favre filtering operation. The variable a may be any scalar field variable such as a species mass fraction Y_k, temperature T and so on. In many reacting LES formulations, a progress variable c is solved for which is used to distinguish fresh (c=0) from burnt gases ($c = 1$), and a model is required for the scalar flux of c, namely f_{ic}. The scalar flux term is particularly important in regions with a low reaction rate. In a premixed flame such a region occurs in the preheat zone of the flame, and the scalar flux term becomes important in determining the correct progress variable variation in this region, which in turn controls the propagation speed of the flame.

In the canonical modelling approach, scalar flux terms are modelled using suitable functions of the resolved (known) quantities such as the Favre-filtered progress

variable and velocity $\tilde{c}$ and $\tilde{u}_i$-these functions usually include gradients of the above quantities also. Many different models have been developed for the scalar flux. Roughly speaking, scalar flux models can be grouped in Eddy Diffusivity models (ED), Structural/Gradient-based models (SG), Transport-Equation-based models (TE), Scale-Similarity models (SS), but also combinations of the above. In the simplest ED models, the scalar flux is modelled using $f_i = -\bar{\rho} D_t \partial \tilde{c} / \partial x_i$ where the turbulent diffusivity D_t is usually calculated assuming a constant Schmidt number $S_c \simeq \nu_t / D_t$, where ν_t is the turbulent viscosity which is estimated from the turbulence model. ED models are simple and easy to implement in LES and provide the necessary dissipation, however they have some important drawbacks. The main drawback lies in the fact that the turbulent diffusivity D_t has no directional dependence. This leads to the scalar flux always being aligned with the gradient of the mean scalar field which is not generally true. For example, in the case of pre-mixed flames, counter-gradient transport is often observed [4]. In order to include anisotropy in the modelling of the scalar flux, Batchelor [5] originally proposed using an anisotropic diffusivity tensor D_{ij} instead. Henceforth, there have been a number of studies employing this approach with varying and often escalating levels of complexity in the evaluation of D_{ij} [6]-[9]. This approach has generally improved the directionality of the scalar flux but not always its magnitude. To this end, dynamic versions of the ED model have also been developed. A very popular dynamic (yet isotropic) model for the scalar flux often used in reacting flow simulations was developed by Moin et al. [10] by extending the dynamic process introduced for the Reynolds stresses by Germano et al. [11]. Dynamic models improve considerably the predictions of the magnitude of the scalar flux, however they may result in significant spatial variations of the models' dynamic parameters. SG models for the scalar flux were developed in analogy to modelling the Reynolds stress term in the work of Clark et al [12] who used a Taylor series expansion of the filter operation in

3

order to approximate the actual un-filtered field. SG models as in [12] include the required anisotropy and were found to provide quantitatively good estimates of the scalar flux in a priori studies. Their performance however in a posteriori studies was generally observed to be poorer in comparison as they did not provide the necessary dissipation. To this end, dynamic but also mixed ED-SG models were developed [13]-[15]. More complex models using the transport equation for the scalar flux term have also been proposed, see for example [16]-[18]. In [16] a generalised scalar flux model was developed based on the assumption of a suitable functional form for the scalar flux. It was shown that ED and SG models are essentially a subset of the more generalised model, something which would explain the improved predictions observed in the case of mixed models. However, the model developed in [16] includes a substantial amount of additional terms which are not all present in the majority of mixed models. This implies that the predictive ability of mixed models lacking some of these terms is limited. At the same time, any model should be relatively simple and easy to implement in practical LES. In that regard, SS-based models are an attractive alternative. In SS-based models the scalar flux is estimated using suitable functions of the filtered and test-filtered values [19]-[21]. SS models however were also found to have a poorer performance in a posteriori studies as compared to a priori studies. As a result, mixed models are again required to provide the necessary dissipation [20]. In the context of premixed reacting flames, a number of different models have also been developed based on the above approaches [4][22]-[26]. Most of these models are additionally modified compared to their non-reacting counter-parts in order to explicitly include the effects of heat release. A detailed a priori analysis of the performance of a number of different scalar flux models in the case of turbulent premixed flames using 1-step chemistry is given in [27]. All the models tested in [27] exhibited significant variations in their predictions, particularly in flames having Lewis numbers (ratio of thermal diffusion rate to mass diffusion rate) Le <1 which

4

showed relatively large discrepancies in comparison with the DNS data.

It is apparent that there exist a multitude of different models for the scalar flux whose complexity and ease of implementation varies substantially. A common characteristic between the majority of the aforementioned models is that they have been developed usually using at least one major simplifying assumption. This may restrict their generality and use. In addition, most of the aforementioned models include parameters/constants whose value greatly affects their performance in addition to the turbulence model used. In the case of dynamic formulations this issue is somewhat alleviated provided the dynamic procedure is suitably defined. This procedure however is not always clear or justifiable and may in some cases be flow-regime and combustion-mode dependent [11].

A different, perhaps more universal and parameter-free modelling approach is based on deconvolution. Deconvolution methods aim to provide an approximation ϕ^* of the original signal ϕ from knowledge of the filtered field $\bar{\phi}$. Hence, functions of ϕ which require modelling e.g. $\overline{y(\phi)}$ may be modelled using $\overline{y(\phi^*)}$ i.e. by explicitly filtering the deconvoluted fields on the LES mesh. Deconvolution methods were introduced in fluid mechanics research in [12, 28]. The SG scalar flux model for example which forms the basis of many mixed models, is essentially a form of deconvolution [12]. In later works, deconvolution was used to provide a model for the Reynolds stresses [29]-[31]. Deconvolution methods were also found to provide good results in wall-bounded flows as well [32] where classic models are notoriously too dissipative. Deconvolution was also recently found to be a powerful tool for complementing physical modelling by directly exploiting the information contained within the resolved signals [33, 34] In the case of reacting flows, deconvolution methods were used both in a priori and a posteriori studies with overall good results [35]-[39]. The focus of these studies in particular has been on deconvoluting the progress variable c or temperature T and species mass fractions Y_k, in order to model the filtered

5

reaction rate $\bar{w}(T^*, Y_k^*)$ in the transport equation for the filtered progress variable.

In the context of modelling the SGS scalar flux term which also appears in the progress variable transport equation, deconvolution may also be an attractive alternative due to its generality and simplicity: deconvolution methods are based on using an inverse filter operation which is mathematically clearly defined. Compared to a scalar-gradient eddy viscosity closure for example, a deconvolution approach does not make any explicit assumption for the Schmidt number, or the form of the turbulent diffusivity tensor. To this end, the aim of this study in particular is to evaluate the performance of an Iterative Deconvolution Method, combined with Explicit Filtering (IDEF) in order to model the scalar flux. The assessment is conducted a priori using DNS data of a freely-propagating turbulent premixed flame in a canonical inflow-outflow configuration. It is important to note at this point that a priori assessments do not guarantee functionality of the models in actual LES. However, in contrast to a posteriori assessments using LES where the influence of modelling and numerical errors are often too difficult to distinguish, a priori assessments involve using direct simulations which are conducted using high-order numerical schemes on fine meshes. This minimises the effect of numerical/discretisation errors and the performance of the models can be clearly evaluated. Another important point to note, is that the majority of a priori assessments in the literature are conducted on the fine DNS mesh-in contrast in order to simulate an actual LES, we conduct the assessment on a much coarser LES mesh which is constructed using the DNS-filtered values on the LES mesh points only. This presents a more stringent a priori assessment, since variable values between the LES mesh points (sub-grid scales) are not known.

The rest of this study is organised as follows: section II gives a short description of the DNS database used, section III presents the filtering and deconvolution operations, and results are discussed in section IV.

6

II.   DESCRIPTION OF THE DNS DATABASE

Direct Numerical Simulations have been conducted using the SENGA2 code [40] which solves the compressible reacting flow Navier-Stokes equations using a 10th order finite difference scheme for interior points, and a 4th order Runge-Kutta scheme for the time-stepping,

$$\frac{\partial \rho}{\partial t} + \frac{\partial \rho u_k}{\partial x_k} = 0 \, , \tag{2}$$

$$\frac{\partial \rho u_i}{\partial t} + \frac{\partial \rho u_k u_i}{\partial x_k} = -\frac{\partial p}{\partial x_i} + \frac{\partial \tau_{ki}}{\partial x_k} \, , \tag{3}$$

$$\frac{\partial \rho E}{\partial t} + \frac{\partial \rho u_k E}{\partial x_k} = -\frac{\partial p u_k}{\partial x_k} - \frac{\partial q_k}{\partial x_k} + \frac{\partial \tau_{km} u_m}{\partial x_k} \, , \tag{4}$$

$$\frac{\partial \rho Y_\alpha}{\partial t} + \frac{\partial \rho u_k Y_\alpha}{\partial x_k} = \dot{w}_\alpha - \frac{\partial \rho V_{\alpha,k} Y_\alpha}{\partial x_k} \, . \tag{5}$$

α is the species identifier and usual notations have been otherwise introduced. A freely-propagating premixed multi-component fuel-air flame in a canonical inflow-outflow configuration is simulated [41]. A detailed chemical mechanism which was developed specifically for such fuels was used, with 49 reactions and 15 species [42, 43]. A turbulent fuel-air mixture flows from one end of the computational domain, burns, and the hot products leave from the other end of the domain.

Table I lists the turbulence parameters for the DNS. Cases A and B were conducted on a (L_x, L_y, L_z) 14x7x7 mm domain, and case C on a 21x7x7 mm domain where y, z are the homogeneous directions, and x is the inhomogeneous direction i.e. the direction of flame propagation. u_{rms} is the rms value of the fluctuating component of the incoming velocity field, with an integral length scale l_{T} on the reactant side. The turbulence Reynolds number is $Re_{\mathrm{T}} = u_{rms} l_{\mathrm{T}} / \nu_r$, the Damkohler number

7

is $Da = (l_{\mathrm{T}}/u_{rms})/(\delta/s_{\mathrm{L}})$ and the Karlovitz number is $Ka = (\delta/\eta_k)^2$, where s_{L} is the laminar flame speed, and the (diffusive) thickness $\delta = \nu_r/s_{\mathrm{L}}$. Note that the laminar flame thickness is defined as $\delta_{\mathrm{L}} = (T_p - T_r)/\max(dT/dx)$ where T_r, T_p are the reactant and product temperatures respectively. These conditions place the flame in the distributed/broken reaction zones regime according to the classic combustion diagram by Peters [44]. Within this regime, the flame no longer appears as a smooth connected surface as in the flamelet regime particularly for the highest turbulence level case: turbulent eddies are able to penetrate the heat-release zone and break apart the flame surface. This presents a challenging environment for the deconvolution method as a result of the presence of many un-connected surfaces in the scalar fields. Further details of the simulations are given in [41].

III.   FILTERING AND DECONVOLUTION OPERATIONS

The DNS data have been explicitly filtered using a Gaussian filter. The filtered value of a variable $\bar{\phi}(\underline{x}, t)$ is defined as,

$$\bar{\phi}(\underline{x}, t) = \int_{\underline{x}'=-\infty}^{\infty} G(\underline{x} - \underline{x}')\phi(\underline{x}', t)d\underline{x}' \tag{6}$$

The filter function is given by,

$$G(\underline{x}) = \left(\frac{6}{\pi\Delta^2}\right)^{\frac{3}{2}} \exp\left(-\frac{6\underline{x} \cdot \underline{x}}{\Delta^2}\right) \tag{7}$$

where Δ is the corresponding filter width. The laminar flame thickness δ_L is used as a basis for filtering at $\Delta^+ = \Delta/\delta_L = 1, 2$ and 3. Note that these choices correspond to filter widths which are significantly larger than the Kolmogorov length scale of the incoming turbulent field. Favre-filtered variables are defined as,

$$\tilde{\phi}(\underline{x}, t) = \frac{\overline{\rho\phi}}{\bar{\rho}} \tag{8}$$

The DNS data have also been filtered for a period of more than 1 flame time $t_{fl} = t/(\delta_{\mathrm{L}}/s_{\mathrm{L}})$ when the flame was fully developed. Average quantities have also been time-averaged over the same period, in order to increase the statistical accuracy of the results.

A number of different deconvolution algorithms have been developed in the literature for solving inverse problems [45, 46]. The filtering operation in LES is a convolution operation between the filter G and the signal ϕ,

$$\bar{\phi}(\underline{x}, t) = \int\limits_{\underline{x}'=-\infty}^{\infty} G(\underline{x} - \underline{x}')\phi(\underline{x}', t)d\underline{x}' = G * \phi(\underline{x}, t) \tag{9}$$

and in Fourier space this becomes,

$$F(\bar{\phi}) = F(G) \cdot F(\phi) \tag{10}$$

where F denotes a Fourier transform. The inverse problem in this case is obtaining an approximation ϕ^* from knowledge of the filtered field values $\bar{\phi}(\underline{x})$. An additional restriction is that the filtered field is known only on the LES mesh which is much coarser than the DNS mesh. In order to simulate this, we define an LES mesh having h/Δ=0.25. This choice is somewhat finer than traditional meshes used in practical LES which typically have h/Δ=1 , however this is necessary so that the filtered fields are accurately resolved on the LES mesh. This is particularly the case for non band-limited signals such as the the progress variable in premixed flames which resembles an error/step function. This point was recently examined in [47] where a simple model for LES mesh requirements for premixed flame simulations was derived. For h/Δ =0.25, this would ensure that the filtered flame thickness is sufficiently resolved

throughout the domain [47]. This may be a strict bound, and in a recent actual LES with deconvolution $h/\Delta =0.5$ has been used instead with overall good results [36] which is a reasonable resolution for an accurate LES simulation. This point leads to a further one: actual LES implementations using deconvolution-based modelling have been conducted for reacting flows, despite any errors/biases introduced by the numerical schemes used in LES.

In order to simulate an LES, the data are first filtered on the fine DNS mesh using Eq. 6. The filtered values on the LES mesh are then extracted from the fine DNS mesh by interpolating the DNS-filtered values onto the LES mesh using high-order Lagrange polynomials. Details of the DNS and LES meshes are given in Table II for cases A and B and in Table III for case C. Note that Δ is normalised with respect to the laminar flame thickness δ_L. Hence, $h = 0.25 \cdot \Delta = 0.25 \cdot \Delta^+ \cdot \delta_L$, and $N_x \cdot h = L_x$ the length of the computational domain as given in the previous section. It is clear that in comparison to the DNS mesh the LES mesh is much coarser. In addition, the spacing in the LES mesh is at most equal to the integral length scale of the incoming turbulence field. With respect to the Komogorov length scale, the LES mesh is much coarser in comparison: the ratio h/η_k for cases A,B and C for the finest LES mesh ($\Delta^+ =1.0$) is 6.8, 14.9 and 20.7 respectively, and much larger for the coarsest LES mesh ($\Delta^+ = 3.0$) considered in this study. Therefore, all small-scale information of the order of the Kolmogorov scale is lost on the simulated LES mesh which presents a challenging environment for the deconvolution method.

Deconvolution using iterative algorithms was used to deconvolute scalar fields such as the species mass fractions and temperature in the case of laminar flames in [38], and for turbulent flames in [39] (on the DNS mesh) with overall good results. The Van Cittert algorithm [48] is a fundamental and simple iterative deconvolution algorithm, which makes it very attractive for practical implementations. In its most basic form the algorithm reads,

$$\phi^{*n+1} = \phi^{*n} + b(\bar{\phi} - G * \phi^{*n}) \tag{11}$$

with $\phi^{*0} = \bar{\phi}$. This is similar to the unsharp masking technique used in image processing for de-blurring images [49]. The classic unsharp masking technique is analogous to one iteration of the Van Cittert algorithm. Many different variations of the algorithm exist, both in constrained and un-constrained forms. In constrained formulations the multiplication factor b is defined so that the deconvoluted variable lies within specified limits [45]. In the case where b is a constant, specific convergence conditions can be derived in the case of periodic signals. Such conditions have been derived in earlier works for general filter functions [50]-in this study specific conditions in the case where G is a Gaussian filter are derived in the Appendix. In the case of a periodic signal we have the result (further details given in the Appendix),

$$\phi^{*n} = \phi + \sum_{r=-\infty}^{\infty} \left(1 - be^{-c_r}\right)^n (\bar{\phi}_r - \phi_r) \tag{12}$$

and the convergence condition on b is,

$$b \begin{cases} b = e^{c_r}, & \text{immediate convergence for wavenumber } r \\ 0 < b < e^{c_r}, & \text{convergence with a non-oscillating reducing sequence for wavenumber } r \\ e^{c_r} < b < 2e^{c_r}, & \text{convergence with an oscillating reducing sequence for wavenumber } r \end{cases} \tag{13}$$

where $c_r = \Delta^2 k_r^2/24$, and where k_r, ϕ_r correspond to the r wavenumber and r wavenumber component of the signal respectively.

The above results show that for a given value of b the deconvolution of large wavenumbers is slower (requiring more iterations n), which is to be expected. Alternatively, for a given number of iterations, larger wavenumbers require a larger

11

correction factor b for convergence. In the case where we choose the convergence to follow a non-oscillating reducing sequence, convergence will be faster for larger values of b (for a particular wavenumber), up until the upper limit e^{c_r} where c_r is non-zero. In the case of signals composed of many different wavenumber components, convergence will be complete for all wavenumbers at a sufficiently large number of iterations provided $0 < b < e^{c_{rmin}}$. This simple result is consistent with previous studies where $b=1$ was used [38, 39]. Clearly, this is a very convenient choice which does not require knowledge of the original wavenumbers contained within the original signal since $b = 1$ is the minimum value of the upper bound e^{c_r} which is not realised since k is non-zero. Hence, $b = 1$ is used throughout this study as well.

A detailed analysis of the error, and of the asymptotic behaviour of this basic form of the deconvolution algorithm, with regards to the energy spectrum of the turbulent kinetic energy is given in [50]. In general, the deconvolution error increases with increasing filter width Δ, and with increasing wave-numbers contained within the original signal (see Appendix). Successive iterations using Eq. (11) will eventually lead to higher-order approximations of the un-filtered signal [45]. However, successive iterations may also enhance the noise components contained within the signal. Hence, in practice, the algorithm should be applied with an error controller in order to limit the number of iterations [46].

A simple error controller is used in this study based on the difference between the filtered signal $\bar{\phi}$ and the explicitly filtered deconvoluted signal $\overline{\phi^*}$. In particular we define,

$$e = < |\bar{\phi}^* - \bar{\phi}| >$$ (14)

where $<>$ denotes a volume-averaging operation over the LES mesh points. This is used as a measure of the accuracy of the deconvoluted signal. In practice, no

12

threshold on this error is implemented, rather the error controller is implemented so that the iteration continues as long as the error e is reducing, with a limit imposed on the maximum number of iterations for every run-this was set to 100 for this study. Under this condition, and for the filter widths tested in this study, the deconvolution process did not incur a significant computational cost. During an actual LES simulation, successive iterations using this method may prove to be computationally more expensive than directly using a classical model for the quantity to be modelled-and this also depends on the complexity of the model (algebraic-based, transport equation-based etc.). Nevertheless, the strength of the deconvolution approach lies in its generality. As a result, it can be used to model additional un-closed terms in the LES equations. In addition, the deconvolution step, which is a series of successive filtering operations, is an ideal candidate for parallelisation using Graphics Processing Units (GPUs): in practice, deconvolution is local to every grid point. All that is needed are the values of the filtered field in the neighbourhood of the grid point i.e. up to a distance of about 2Δ in every direction where the filter value essentially drops to zero relative to its maximum (center-point) value. This process would render the deconvolution step computationally efficient for use in LES.

In essence, the deconvolution-based scalar flux model is similar to a scale-similarity model: successive iterations using Eq. 11 lead to more accurate predictions of the unfiltered field by the addition of successively filtered corrections:

$$\phi^1 = \bar{\phi} + b(\bar{\phi} - \bar{\bar{\phi}})$$
$$\phi^2 = \bar{\phi} + 2b(\bar{\phi} - \bar{\bar{\phi}}) + b^2(\bar{\bar{\bar{\phi}}} - \bar{\bar{\phi}})$$

$$(15)$$

13

Most SGS closures are designed to operate with the cut-off length scale lying within the inertial range where the scale-similarity assumption is likely to be valid. This fine point reinforces the idea that the resolution level should be high enough for deconvolution to be valid. Another important point to note is that the method is consistent in the limit of zero filter width since at this limit Eq. (11) recovers the DNS result-starting from the initial guess then by definition the term in parenthesis will be zero.

IV. SCALAR FLUX MODELLING

In the case of variable density flows, the available variables from the LES would be $\bar{\rho}$ and $\overline{\rho\phi}$. Hence, scalar fields are recovered from Favre-averaged variables using,

$$\phi^*(\underline{x},t) = \frac{\{\rho(\underline{x},t)\phi(\underline{x},t)\}^*}{\rho^*(\underline{x},t)} \tag{16}$$

where function approximations are denoted by an asterisk. The deconvoluted field is then explicitly filtered to recover estimates of any filtered variable in question e.g.

$$\tilde{\phi}^*(\underline{x},t) = \frac{\overline{\{\rho(\underline{x},t)\phi(\underline{x},t)\}^*}}{\bar{\rho}(\underline{x},t)} \tag{17}$$

In order to model the scalar flux, we begin from the available solution variables from the LES: these are $\bar{\rho}$, $\overline{\rho u_i}$ and $\overline{\rho c}$. These are calculated by filtering ρ, ρu_i and ρc on the DNS mesh, and then sampling them using interpolation to obtain their values on the coarse LES mesh. Deconvolution (Eq. 11) is then applied to $\bar{\rho}$, $\overline{\rho u_i}$ and $\overline{\rho c}$ on the LES mesh in order to recover estimates of ρ, ρu_i and ρc on the LES mesh namely ρ^*, $\{\rho u_i\}^*$ and $\{\rho c\}^*$. Note that the deconvolution step is conducted in 3D space and that the same filter is used both in the filtering and deconvolution steps. Once these estimates are obtained, an estimate of the product $\rho u_i c$ on the LES mesh

14

is calculated using ${\rho u_i c}^* = {\rho u_i}^* \cdot {\rho c}^*/\rho^*$. The scalar flux can then be modelled using,

$$f_i^{IDEF} = \bar{\rho} \left(\overline{{\rho u_i c}^*}/\bar{\rho} - \tilde{u}_i \tilde{c} \right) = \bar{\rho} \left(\widehat{{u_i c}}^* - \tilde{u}_i \tilde{c} \right) \tag{18}$$

where the filtering is conducted on the coarse LES mesh as would be the case in actual LES, and not on the fine DNS mesh. Note that the progress variable c is based on temperature i.e. $c = (T - T_r)/(T_p - T_r)$.

In order to illustrate the process, consider the deconvolution of $\overline{\rho u c}$ for the highest turbulence level, case C, shown in Figure 1. Figure 1 (a) shows instantaneous x, y snapshots of the original un-filtered DNS field $\rho u c$ sampled onto the LES mesh-this and all other fields in the rest of the images are normalised using the maximum instantaneous DNS value found in Fig. 1 (a) in order to warrant a fare comparison. Reactants flow from the bottom of the figures, burn, and the hot products leave from the top end of the domain. The second column of images in Fig. 1 shows the filtered field $\overline{\rho u c}$, on the LES mesh, for $\Delta^+ = 1$, 2 and 3 respectively. Filtering has a major effect for this term, and as one may observe from the second column of images (b), (e), and (h), much of the small-scale features at the leading edge of the flame front are lost, and this effect is more pronounced as expected as the filter width increases. The third column of images in Fig. 1, shows the deconvoluted field ${\rho u c}^*$ as obtained on the LES mesh using Eq. 11 and the process outlined in the previous paragraph. For $\Delta^+ = 1$, deconvolution is very accurate and produces a field ${\rho u c}^*$ which is almost in perfect agreement with the DNS field just by visual inspection. For $\Delta^+ = 2$ and 3, deconvolution performs poorer in comparison as expected: note in particular that for $\Delta^+ = 3.0$ the finer scales at the leading edge of the flame front i.e. close to the cold side (blue side) are not as accurately recovered. This result is in agreement with the prediction of Eq. 13 since a larger c_r value implies slower

15

convergence for the same number of iterations. The larger-scale structures however found in the products' side (red side) are recovered to a very good degree. Finally, the last column of images in Fig. 1, shows the filtered-deconvoluted field $\overline{\{\rho uc\}^*}$, on the LES mesh, obtained by filtering the deconvoluted field in the third column of images. It is clear that for all filter widths considered, the last column of images is in very good agreement with the second column of images.

Figure 2 shows the effect of devonvolution between successive iterations up to the threshold value of 100 set in this study. Figure 2 (a), shows the filtered field $\overline{\rho uc}$ for a filter having $\Delta^+ =2.0$. Going from left to right during the deconvolution iteration, one obtains successively more accurate (finer) approximations of the original un-filtered field. This is more pronounced at the reactants' side where smaller-scale structures are found.

In order to benchmark the performance of the IDEF-based model against more established models in the literature we also calculate scalar flux predictions using the Clark model,

$$f_i^{Clark} = \bar{\rho}\frac{\Delta^2}{12}\frac{\partial \tilde{u}_i}{\partial x_j}\frac{\partial \tilde{c}}{\partial x_j} \tag{19}$$

This model was found in [27] to provide overall the highest correlations against the DNS data in the case of a 1-step chemistry premixed flame, hence it is used here as a benchmark model. It is important to note however that the evaluation of this model in [27] was conducted on the DNS mesh in contrast with the evaluation in this study which is conducted on a much coarser simulated LES mesh.

In order to quantify the performance of the above models we examine two different quantities: a) the actual flux in the (inhomogeneous) direction of mean flow x i.e. f_1, and b) the divergence of the flux $F = \partial f_i/\partial x_i$. The scalar flux in the mean direction of flow propagation f_1 is the dominant term since this is also the mean direction

16

of flame propagation and there are large gradients in the progress variable c in this direction. The divergence of f on the other hand F, allows us to: (a) examine the collective ability of the model in modelling the scalar flux terms in the two other homogeneous directions y, z as well, and (b) to determine whether the gradients of the scalar flux are accurately recovered in addition to its actual local magnitude. Note that in an actual LES the term $(-F)$ would be the one contributing to the right-hand side of the transport equation for the filtered progress variable [23].

The data are averaged in the homogeneous directions y, z at every point in the direction of the mean incoming turbulent velocity field x. For any variable v we have,

$$v_x(i) = \frac{1}{N_y N_z} \sum_{j,k} v(x_i, y_j, z_k) \tag{20}$$

where N_y, N_z are the number of LES mesh points in the y, z directions respectively as given in Tables II and III for the different filter widths. A correlation coefficient is also used in order to quantify the local spatial agreement between the modelled variable and the actual variable as obtained from the DNS. For any two variables x, y this is defined as,

$$R(x, y) = \frac{\sum_{i=1}^{N}(x_i - \bar{x}_i)(y_i - \bar{y}_i)}{\sqrt{\sum_{i=1}^{N}(x_i - \bar{x}_i)^2}\sqrt{\sum_{i=1}^{N}(y_i - \bar{y}_i)^2}} \tag{21}$$

where the overbar in Eq. 21 denotes the sample mean and not filtering. The correlation coefficients for any two quantities are calculated at every time-step and are time-averaged over successive instances in order to increase the statistical accuracy of the results.

Figures 3 (a) and 3 (b) show instantaneous values of the scalar flux component f_1 as predicted using the IDEF method and Clark's model against the DNS values for the lowest turbulence level case A, for $\Delta^+=1$. Both the DNS values and the models'

17

predictions are normalised using the maximum instantaneous f_1 value as obtained from the DNS. It is clear that there is a strong correlation both for the IDEF-based model and the Clark model. Figures 4(a) and 4(b) show the models' predictions in the case $\Delta^+=3$ instead. Both models again appear to retain strong correlations against the DNS data despite the larger filter width.

Figures 5(a) and 5(b) show the instantaneous predictions of the IDEF and Clark models against the DNS result for the highest turbulence level instead, case C, at $\Delta^+ =1$. The correlations for this case deteriorate for both models in comparison with the lower turbulence level case A. In the case of the IDEF method, the highest turbulence level implies larger wavenumbers in the original field are to be deconvoluted. Since the IDEF method is applied with a maximum iteration limiter, these wavenumbers are not recovered as accurately which explains the deterioration in the correlation. In the case of the Clark model, the coarse LES mesh may not be sufficient for the derivatives which appear in Eq. 19 to be accurately calculated. The same is also true if a larger filter width is used as one may observe from the results in Figs. 6(a) and 6(b) which show the models' predictions in the case where $\Delta^+=3$ instead. The Clark model is found to perform less well in comparison to the IDEF-based model which appears to have an improved correlation (though weak) with the DNS data. The Clark model appears to under-estimate, on average, the magnitude of the scalar flux term in regions with negative flux: the coarse mesh implies the derivatives appearing in Eq. 19 are under-estimated which would explain this behaviour.

Figures 7, 8 and 9 (a)-(c) show the y, z-averaged values of the scalar flux component in the direction of mean inflow (f_{1x}) obtained using Eq. 20 for cases A,B and C, for the filter widths $\Delta^+ = 1,2$ and 3, respectively. These are normalised using the reactant's density ρ_r and the laminar flame speed s_l. It is important to note the difference in scalar flux behaviour between case A, and cases B and C: case A

18

exhibits counter-gradient behaviour while cases B and C exhibit gradient behaviour. A scalar flux model should be able to capture both types of behaviour and classic gradient-type models for the scalar flux predict only one of the two. The x-axis corresponds to the y, z-averaged value of the Favre-filtered progress variable $\tilde{c}_x$. For case A and for $\Delta^+=1$ shown in Fig. 7 (a), both the IDEF and Clark models show a very good agreement with the DNS data. For $\Delta^+=2$ and 3 shown in Figs. Fig. 7 (b) and (c), the Clark model shows a poorer performance while the IDEF model provides a relatively improved prediction. For the intermediate turbulence level case B, the Clark model shows a poor agreement as one may observe from the results in Figs. 8 (a)-(c): the magnitude of the scalar flux is under-estimated for all filter widths considered. This is somewhat in contrast to the results in [27] where a relatively better agreement was observed for the Clark model for all filter widths considered, however the evaluation in [27] was conducted on the DNS mesh in contrast with the evaluation in this study which is conducted on a simulated LES mesh which is much coarser. Hence, gradients in the Clark model are not calculated on the fine DNS mesh which would explain the difference. This point would also explain the good agreement observed for the Clark model in a priori studies, but the poorer agreement observed in a posteriori studies which are conducted on the coarser LES mesh [15, 28]. The IDEF model on the other hand, shows good agreement with the DNS results for all filter widths both in the case of gradient and counter-gradient flux behaviour. An additional point to note is that such a priori studies where simulated LES meshes are used can be useful to elucidate such differences in models' performance. For the highest turbulence level case C, a similar trend is observed. Figures 9 (a)-(c) show that for small filter widths the IDEF method provides quantitatively good estimates of the scalar flux component f_1, while the Clark model performs less well in comparison. For $\Delta^+ =3$ the IDEF method shows poorer agreement particularly in the region $0.5 < \tilde{c}_x < 1.0$ approximately, where there is a clear over-estimation of the scalar

flux. This is owing to insufficient resolution due to the coarse mesh in this region of the flame brush where the density drops and the flow accelerates towards the burnt products. This transition is not captured on the LES mesh hence the deconvolution is unable to recover the un-filtered field in this part of the flame.

Figures 10, 11 and 12 (a)-(c) show the y, z averages, calculated using Eq. 20, for the divergence of the scalar flux $F = \partial f_i / \partial x_i$, for cases A,B and C respectively. This is normalised using the reactant's density and laminar flame speed only (dimensions are inverse length) for convenience with plotting. Tables IV and V show in addition the relevant correlation coefficients for the two models for this term. As the divergence term includes contributions from the scalar fluxes in the y, z directions it functions as a good marker of the overall performance of a scalar flux model. For case A both models show a good agreement with the DNS data for all filter widths considered as one may observe from the results in Figs. 10 (a)-(c). This is also reflected in the near- unity correlation coefficients which are listed in Tables IV and V, for this case. For the intermediate turbulence level case B, significant differences are observed between the two models: the IDEF-based model provides good predictions of the divergence of the scalar flux F for all filter widths considered while the Clark model provides a poorer agreement in comparison. Tables IV and V also show relatively poorer correlation coefficients for the Clark model. For the highest filter width considered i.e. $\Delta^+=3$, and for the highest turbulence level case C, the IDEF model is found to give a reasonable prediction of F despite the poorer agreement for the $x-$component of the flux in Figure 7 (c). The correlation coefficients are also larger in comparison than the Clark model correlations. In agreement with the results in Fig. 9 the Clark model under-estimates the magnitude of F-this may be a result of the coarser LES mesh which gives rise to lower values of the calculated spatial derivative product term $(\partial u_i / \partial x_j)(\partial c / \partial x_j)$ of the model. This is where modifications of the Clark model such as dynamic or mixed models would be required in

20

order to provide the necessary dissipation [14, 15].

V.   CONCLUSIONS

A three-dimensional direct numerical simulation database of a turbulent premixed flame is used in order to assess the performance of a deconvolution-based model for the scalar flux of the progress variable $\bar{\rho}(\widetilde{u_i c} - \tilde{u}_i \tilde{c})$, in the context of LES.

The DNS data are first filtered on the fine DNS mesh and are then sampled on the much coarser LES mesh. An iterative deconvolution algorithm is then used in order to provide estimates of the values of the original (un-filtered) fields on the LES mesh. The deconvolution estimates are then explicitly filtered on the coarser LES mesh using the same filter in order to provide an estimate of the scalar flux. This procedure is thus more stringent than the procedure followed in classical a priori tests where the models' performance is evaluated directly on the fine DNS mesh where all sub-grid scale information is available.

For the filter widths considered in this study, deconvolution is found to provide improved estimates of the scalar flux in comparison to a classic model which is known to provide good results in a priori studies for turbulent premixed flames. This includes both average quantities but also local quantities with relatively high correlation coefficients, both for gradient and counter-gradient-type scalar flux behaviour. The deconvolution process appears to be less sensitive to the filter width variation, and since the method does not explicitly involve any tunable parameters/constants this implies the method can be applied to different flow regimes and combustion modes. The method does involve an integration operation over the filtered field values which implies sufficient resolution on the LES mesh is required for the filtered fields to be accurately deconvoluted.

As highlighted in the introduction, it is important to note again that any priori

21

validation of a sub-grid scale model does not guarantee functionality in actual LES. However, recent implementations of deconvolution in reacting LES with overall good results [32, 35, 36], are indicative of the merit of this modelling approach.

ACKNOWLEDGMENT

Appendix: Convergence conditions for a Gaussian filter function.

Consider a periodic 1D function given by,

$$\phi(x) = \sum_{r=-\infty}^{\infty} a_r e^{ik_r x}$$

where k_r are the corresponding wavenumbers. We will assume that the function extends in an unbounded domain. Since the filtering operation as defined by Eq. 6 is linear we have,

$$\bar{\phi}(x) = \sum_{r=-\infty}^{\infty} a_r e^{-c_r} e^{ik_r x}$$

where $c_r = \Delta^2 k_r^2/24$. Now let,

22

$$\phi^{*n} = \sum_{r=-\infty}^{\infty} A_r{}^n e^{ik_r x}$$

where the coefficients $A_r{}^n$ are to be determined. Then we have,

$$G * \phi^{*n} = \overline{\phi^{*n}} = \sum_{r=-\infty}^{\infty} A_r{}^n e^{-c_r} e^{ik_r x}$$

Van Cittert's algorithm reads $\phi^{*n} = \phi^{*n} + b(\bar{\phi} - G * \phi^{*n})$. Inserting the above results into Van Cittert's algorithm we have,

$$\sum_{r=-\infty}^{\infty} A_r{}^{n+1} e^{ik_r x} = \sum_{r=-\infty}^{\infty} A_r{}^n e^{ik_r x} + b\left(\sum_{r=-\infty}^{\infty} a_r e^{-c_r} e^{ik_r x} - \sum_{r=-\infty}^{\infty} A_r{}^n e^{-c_r} e^{ik_r x} \right)$$

Equating the coefficients,

$$A_r{}^{n+1} = A_r{}^n \left(1 - be^{-c_r} \right) + ba_r e^{-c_r}$$

which is a geometric series with the solution,

$$A_r{}^n = a_r + \left(1 - be^{-c_r} \right)^n (A_r{}^0 - a_r)$$

The solution at the n_{th} iteration is then given by,

$$\phi^{*n} = \sum_{r=-\infty}^{\infty} a_r e^{ik_r x} + \left(1 - be^{-c_r} \right)^n (A_r{}^0 - a_r) e^{ik_r x} \tag{A.1}$$

$$= \phi + \sum_{r=-\infty}^{\infty} \left(1 - be^{-c_r} \right)^n (\bar{\phi}_r - \phi_r) \tag{A.2}$$

where ϕ_r corresponds to the r wavenumber component of the signal. For convergence we require,

23

$$-1 < \left(1 - be^{-c_r}\right) < 1 \tag{A.3}$$

which sets bounds on the value of the constant b for a given wavenumber r as follows,

$$b \begin{cases} b = e^{c_r}, & \text{immediate convergence for wavenumber } r \\ 0 < b < e^{c_r}, & \text{non-oscillating reducing sequence for wavenumber } r \\ e^{c_r} < b < 2e^{c_r}, & \text{oscillating reducing sequence for wavenumber } r \end{cases}$$

Case	u_{rms}/s_L	l_T/δ	Re_T	Da	Ka
A	3.18	16.54	52.66	5.19	1.39
B	9.00	16.66	150.05	1.85	6.62
C	14.04	16.43	230.69	1.17	12.97

TABLE I: Turbulent flame parameters for the DNS cases.

Δ^+	N_x	N_y	N_z	h/l_T
DNS	768	384	384	0.03
1	74	37	37	0.35
2	37	18	18	0.69
3	24	12	12	1.04

TABLE II: DNS and LES meshes for cases A and B with $h/\Delta = 0.25$.

Δ^+	N_x	N_y	N_z	h/l_T
DNS	1632	544	544	0.02
1	112	37	37	0.21
2	56	18	18	0.42
3	37	12	12	0.64

TABLE III: DNS and LES meshes for case C with $h/\Delta = 0.25$.

$\Delta^+/R(F^{IDEF}, F)$	A	B	C
1	0.9746	0.9704	0.9459
2	0.8852	0.9155	0.8609
3	0.8751	0.8302	0.7777

TABLE IV: Global time-averaged Pearson correlation coefficients for F using IDEF.

$\Delta^+/R(F^{Clark}, F)$	A	B	C
1	0.9597	0.9122	0.9085
2	0.8919	0.7596	0.7661
3	0.8694	0.4849	0.6118

TABLE V: Global time-averaged Pearson correlation coefficients for F using Clark's model.
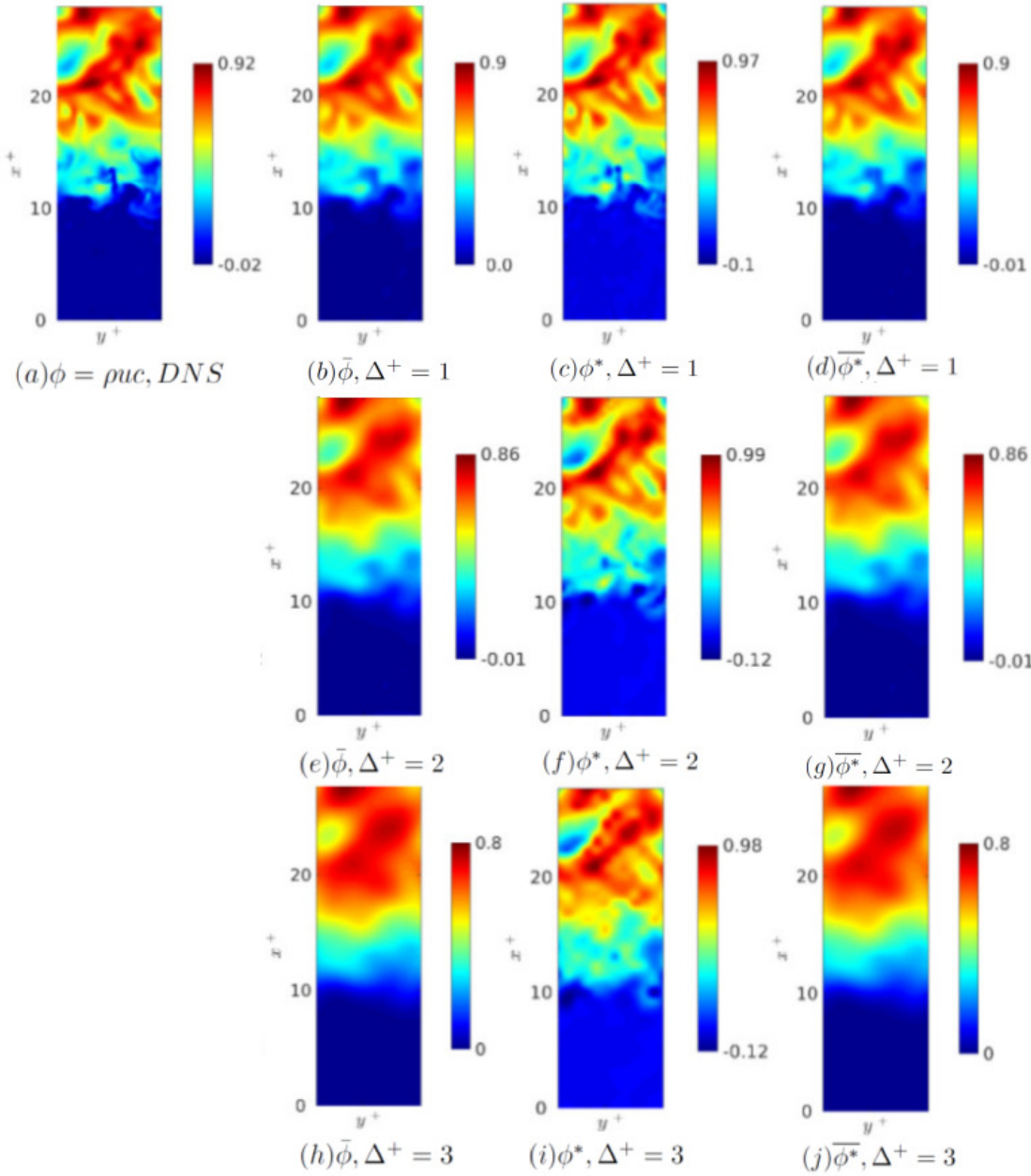
FIG. 1. The deconvolution/explicit-filtering process applied to $\bar{\phi} = \overline{\rho u c}$. Going from left to right are the original DNS field (a) $\rho u c$, the filtered field $\overline{\rho u c}$, the deconvoluted field $\{\rho u c\}^*$, and the filtered-deconvoluted field $\overline{\{\rho u c\}^*}$ for each filter in (b)-(j). The data correspond to an instantaneous snapshot in the z direction for case C, and are normalised using the maximum instantaneous DNS value. Reactants flow from the bottom and hot products exit from the top. Note that deconvolution is conducted in 3D-the figures are simply 2D contours.
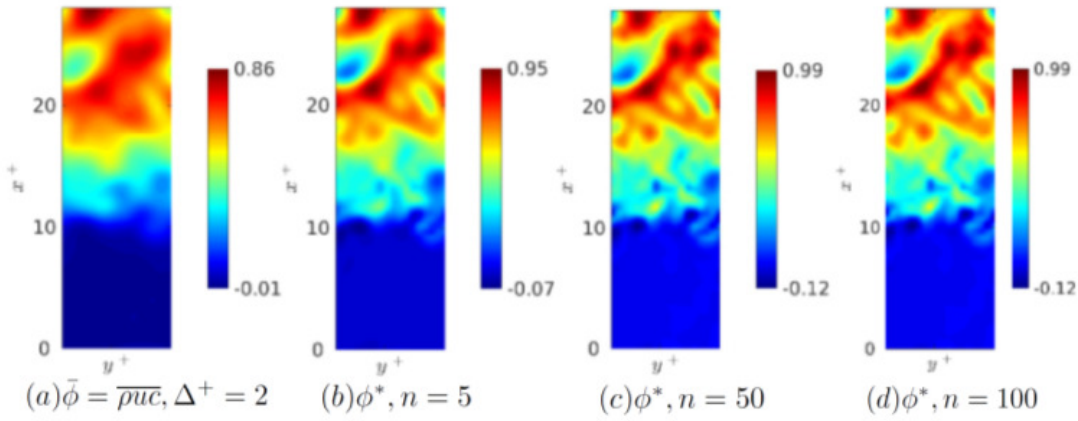
FIG. 2. Sample output from successive iterations n using the deconvolution algorithm. Starting from the left is the filtered field (a) $\bar{\phi} = \overline{\rho u c}$ for $\Delta^+ = 2.0$, and moving to the right (b)-(d) are the deconvoluted fields on the LES mesh. Notice the gradual sharpening of the image as smaller-scale structures are recovered particularly in the reactants side (blue side).
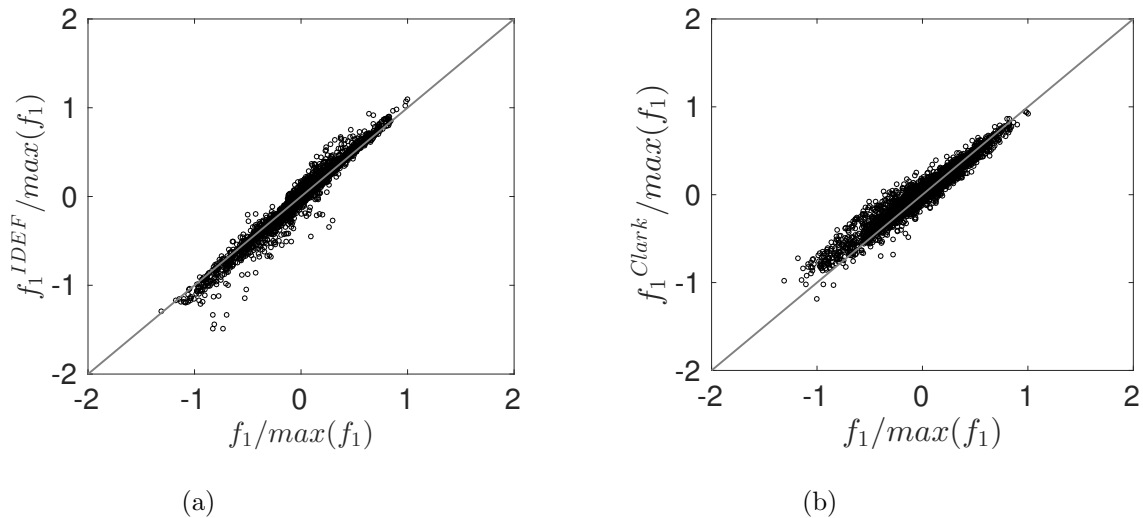
FIG. 3. Case A instantaneous scatter plot of x-component of the scalar flux term, f_1, against the DNS result for $\Delta^+ =1.0$: (a) using IDEF and (b) using Clark's model.
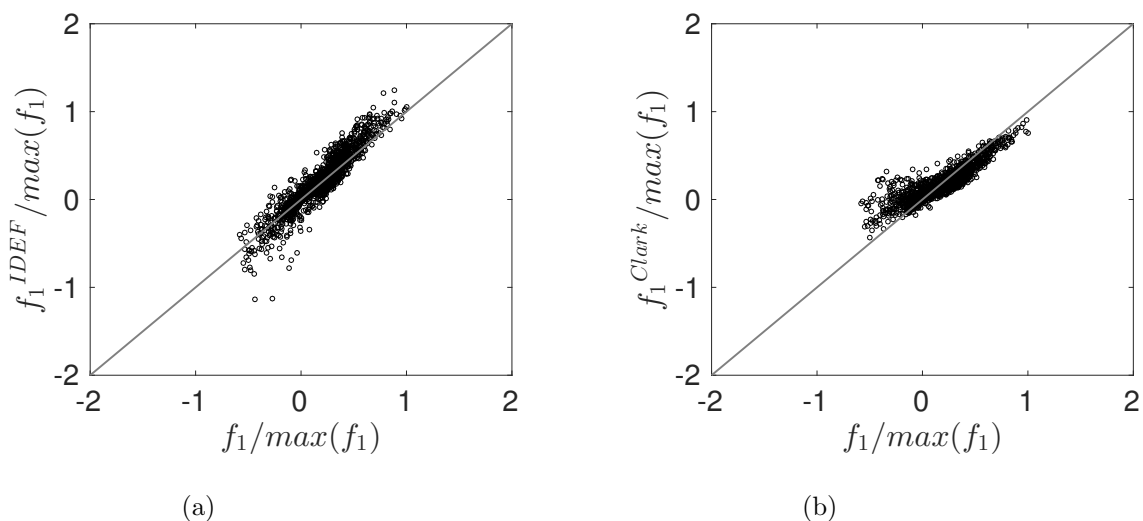
FIG. 4. Case A instantaneous scatter plot of x-component of the scalar flux term, f_1, against the DNS result for $\Delta^+ =3.0$: (a) using IDEF and (b) using Clark's model.
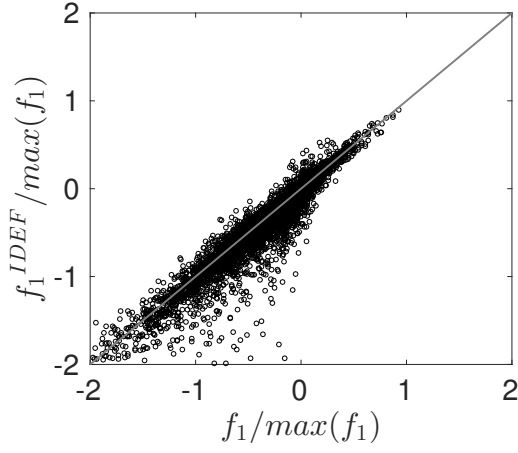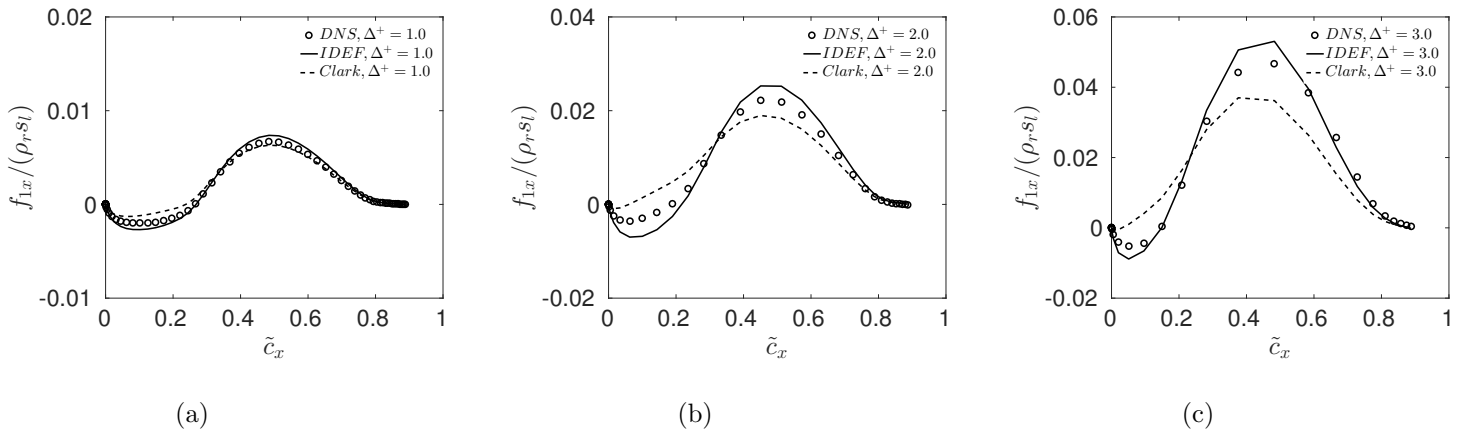
(a)
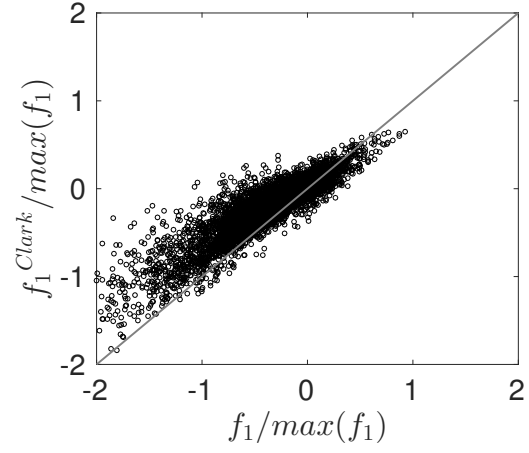
(b)

FIG. 5. Case C instantaneous scatter plot of x-component of the scalar flux term, f_1, against the DNS result for $\Delta^+ = 1.0$: (a) using IDEF and (b) using Clark's model.
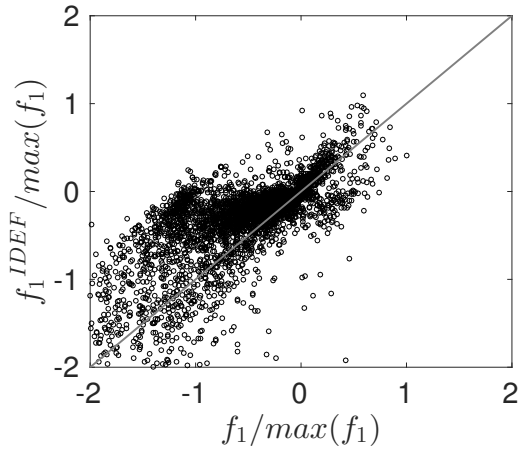
(a)
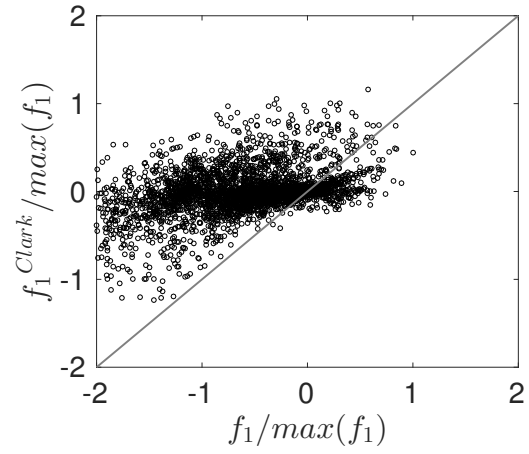
(b)

FIG. 6. Case C instantaneous scatter plot of x-component of the scalar flux term, f_1, against the DNS result for $\Delta^+ = 3.0$: (a) using IDEF and (b) using Clark's model.

FIG. 7. Averaged (in homogeneous directions y, z) flux term f_{1x} for case A: (a) $\Delta^+=1$, (b) $\Delta^+=2$, (c) $\Delta^+=3$.
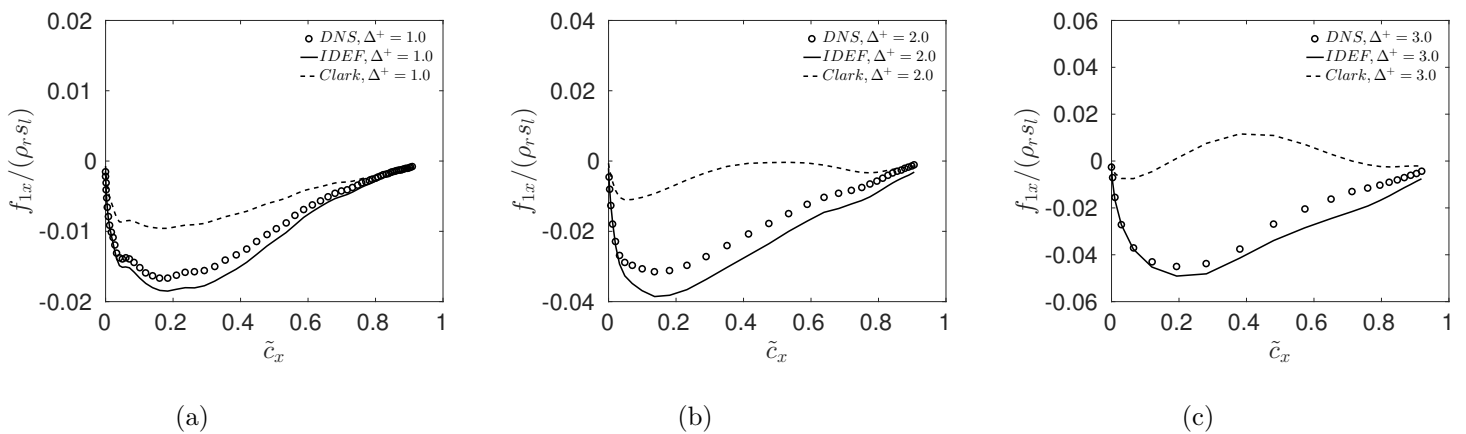
FIG. 8. Averaged (in homogeneous directions y, z) flux term f_{1x} for case B: (a) $\Delta^+=1$, (b) $\Delta^+=2$, (c) $\Delta^+=3$.
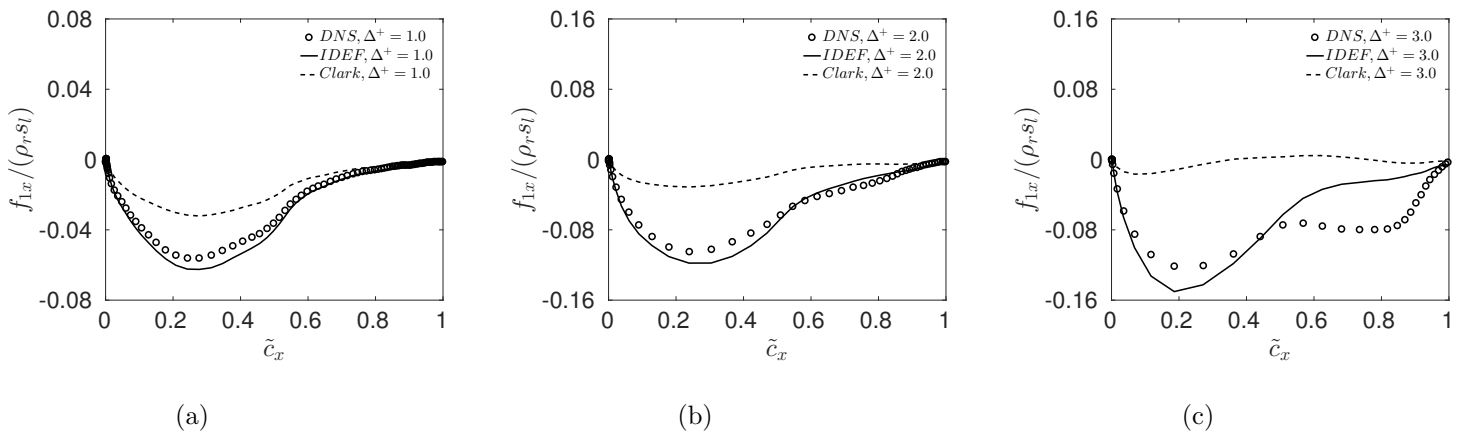

FIG. 9. Averaged (in homogeneous directions y, z) flux term f_{1x} for case C: (a) $\Delta^+=1$, (b) $\Delta^+=2$, (c) $\Delta^+=3$.
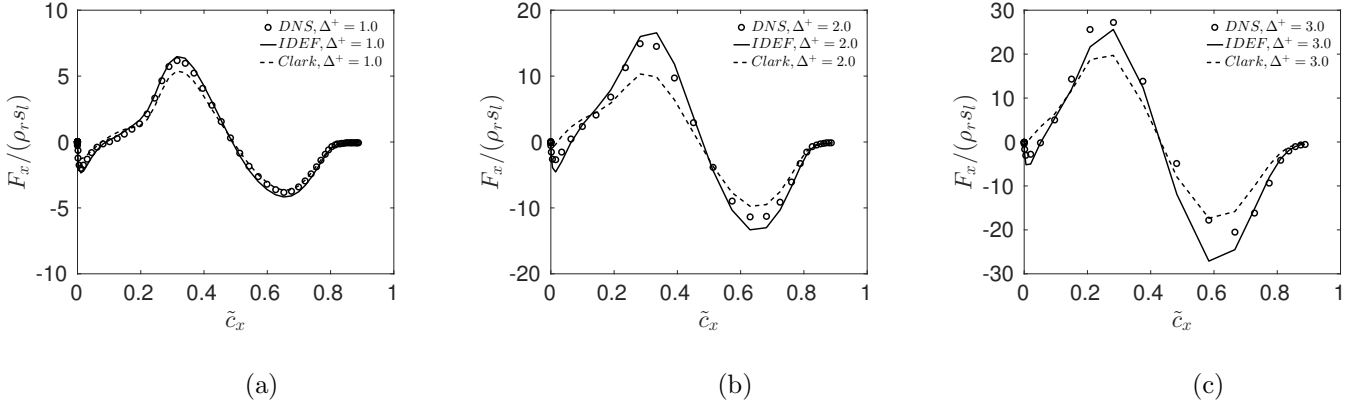
FIG. 10. Averaged (in homogeneous directions y, z) flux term F_x for case A: (a) $\Delta^+=1$, (b) $\Delta^+=2$, (c) $\Delta^+=3$.
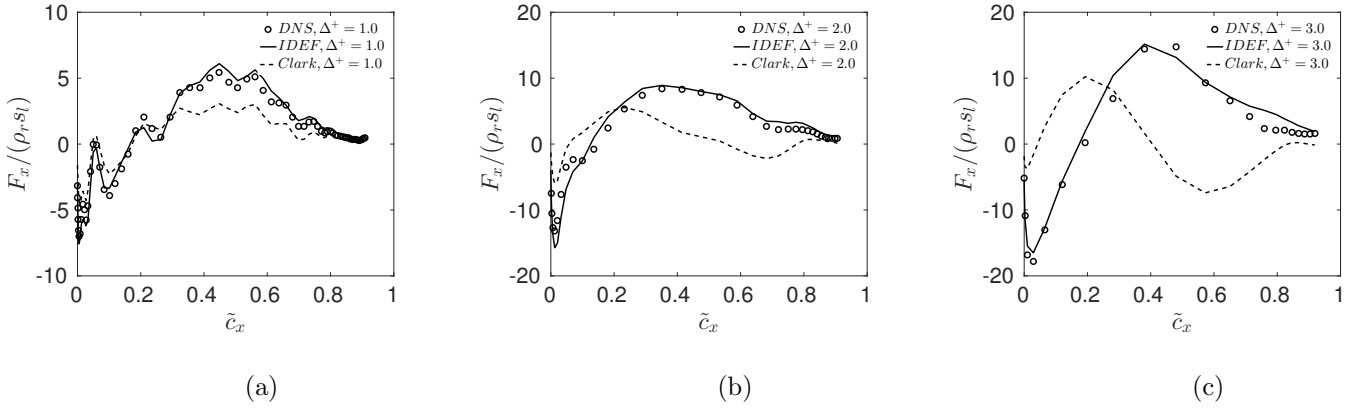

FIG. 11. Averaged (in homogeneous directions y, z) flux term F_x for case B: (a) $\Delta^+=1$, (b) $\Delta^+=2$, (c) $\Delta^+=3$.
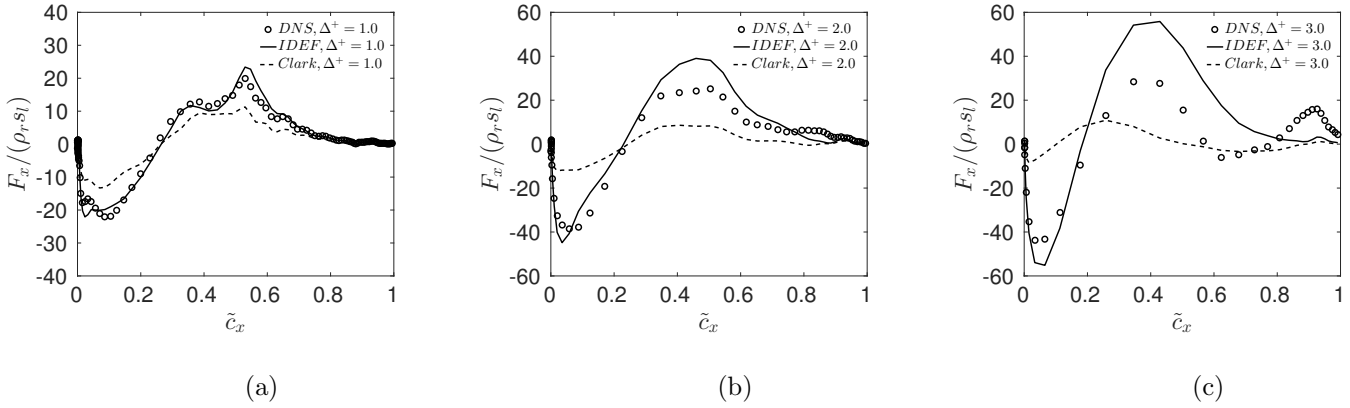

FIG. 12. Averaged (in homogeneous directions y, z) flux term F_x for case C: (a) $\Delta^+=1$, (b) $\Delta^+=2$, (c) $\Delta^+=3$.

[1] L. Y. M. Gicquel, G. Staffelbach, T. Poinsot, Large eddy simulations of gaseous flames in gas turbine combustion chambers, Prog. En. Combust. Sc. 38, 782 (2012).

[2] H. Pitsch, Large eddy simulation of turbulent combustion, Ann. Rev. Fluid Mech. 38, 453 (2006).

[3] P. Sagaut, Large Eddy Simulation for Incompressible Flows: An Introduction, 2nd Edition Springer-Verlag (2001).

[4] K.N.C. Bray, P.A. Libby, J.B. Moss, Unified modelling approach for premixed turbulent combustion Part I: general formulation, Combust. Flame 61, 87 (1985).

[5] G.K. Batchelor, Diffusion in a field of homogeneous turbulence, Austr. J. Sci. Res. Series A2, 437 (1949).

[6] B.J. Daly, F.H. Harlow, Transport equations in turbulence, Phys. Fluids 13, 2634 (1970).

[7] Y. Shabany, P.A. Durbin, Explicit Algebraic Scalar Flux Approximation, AIAA 35, 985 (1997).

[8] K. Abe, K. Suga., Large eddy simulation of passive scalar fields under several strain conditions, Proc. Turb. Heat Transf. II, Manchester May 31-June 5, 8 (1998).

[9] S. Chumakov, A priori study of subgrid-scale flux of a passive scalar in isotropic homogeneous turbulence, Phys. Rev. E 78 036313 (2008).

[10] P. Moin, K. Squires, W. Cabot, S. Lee. A dynamic subgridscale model for compressible turbulence and scalar transport, Phys. Fluids 3, 2746 (1991).

[11] M. Germano, U. Piomelli, P. Moin, W.H. Cabbot, A dynamic sub-grid eddy viscosity model. Phys. Fluids A 3(7), 1760 (1991).

[12] R.A. Clark, Evaluation of sub-grid scalar models using an accurately simulated turbulent flow. J. Fluid Mech. 91, 1 (1979).

[13] B. Vreman, B. Geurts, H. Kuerten, Large-eddy simulation of the turbulent mixing layer, J. Fluid Mech. 339, 357 (1997).

[14] Y. Fabre, G. Balarac, Development of a new dynamic procedure for the Clark model of the subgrid-scale scalar flux using the concept of optimal estimator, Phys. Fluids 23, 115103-1 (2011).

[15] G. Balarac, J. Le Sommer, X. Meunier, A. Vollant, A dynamic regularized gradient model of the subgrid-scale scalar flux for large eddy simulations, Phys. Fluids 25, 075107 (2013).

[16] B.A. Younnis, C.G. Speziale, T.T. Clark. A rational model for the turbulent scalar fluxes, Proc. R. Soc. A 461, 575 (2005).

[17] A.V. Johansson, P.M. Wikstrom, DNS and modelling of passive scalar transport in turbulent channel flow with a focus on scalar dissipation rate modelling, Flow Turb. Combust. 53, 223 (1999).

[18] P.M. Wikstrom, S. Wallin, A.V. Johansson, Derivation and investigation of a new explicit algebraic model for the passive scalar flux, Phys. Fluids 12, 688 (2000).

[19] J. Bardina, J. H. Ferziger, W. C. Reynolds, Improved subgrid scale models for large eddy simulation, AIAA 80-1357 (1980).

[20] B.W. Anderson, J.A. Domaradzki, A subgrid-scale model for large-eddy simulation based on the physics of interscale energy transfer in turbulence, Phys. Fluids 24, 065104-1 (2012).

[21] S.G. Chumakov, C.J. Rutland. Dynamic structure subgrid-scale models for large eddy simulation, Int. J. Numer. Methods Fluids 47, 911 (2005).

[22] D. Veynante, A. Trouve, K.N.C. Bray, T. Mantel, Gradient and counter-gradient turbulent scalar transport in turbulent premixed flames, J. Fluid Mech. 332, 263 (1997).

[23] M. Boger, D. Veynante, H. Boughanem, A. Trouv, Direct Numerical Simulation anal-

ysis of flame surface density concept for Large Eddy Simulation of turbulent premixed combustion, Proc. Combust. Inst. 27, 917 (1998).

[24] H.G. Weller, G. Tabor, A.D. Gosman, C. Fureby, Application of flame wrinkling LES combustion model to a turbulent mixing layer, Proc. Combust. Inst. 27, 899 (1998).

[25] S. Richard, O. Colin, O. Vermorel, C. Angelberger, A. Benkenida, D. Veynante, Large eddy simulation of combustion in spark ignition engine, Proc. Combust. Inst. 31, 3059 (2007).

[26] S.W. Tullis, R.S. Cant, Scalar transport modeling in large eddy simulation of turbulent premixed flames, Proc. Combust. Inst. 29, 2097 (2004).

[27] Y. Gao, N. Chakraborty, M. Klein. Assessment of the performances of sub-grid scalar flux models for premixed flames with different global Lewis numbers: A Direct Numerical Simulation analysis, Int. J. Heat Fluid Fl. 52, 28 (2015).

[28] A. Leonard, Energy cascade in large eddy simulation of turbulent fluid flows, Adv. Geophys., 18A, 237 (1974).

[29] B.G. Geurts, Inverse modeling for large-eddy simulation, Phys. Fluids 9, 3585 (1997).

[30] J.A. Domaradzki, E.M. Saiki, A subgrid-scale model based on the estimation of unresolved scales of turbulence, Phys. Fluids 9, 2148 (1997).

[31] S. Stolz, N. Adams, An approximate deconvolution procedure for large-eddy simulation, Phys. Fluids 11, 1699 (1999).

[32] S. Stolz, N. Adams, An approximate deconvolution model for large-eddy simulation with application to incompressible wall-bounded flows, Phys. Fluids 13, 997 (2001).

[33] S. Bose, P. Moin, A dynamic slip boundary condition for wall-modeled large-eddy simulation, Phys. Fluids 26, 015104-1 (2014).

[34] C. Locci, L. Vervisch, Eulerian scalar projection in Lagrangian point source context: An approximate inverse filtering approach, Flow Turb. Combust. 97, (2016).

[35] J. Mathew, Large Eddy Simulation of a premixed flame with approximate deconvolu-

tion modelling, Proc. Combust. Inst. 29, 1995 (2002).

[36] P. Domingo, L. Vervisch, Large eddy simulation of premixed turbulent combustion using approximate deconvolution and explicit flame filtering, Proc. Combust. Inst. 35, 1349 (2015).

[37] P. Domingo, L. Vervisch, DNS and approximate deconvolution as a tool to analyse one-dimensional filtered flame sub-grid scale modelling, Combust. Flame 177, 109 (2017).

[38] C. Mehl, J. Idier, B. Fiorina B., Evaluation of deconvolution modelling applied to numerical combustion, Combust. Th. Model. (2017), DOI:10.1080/13647830.2017.1358405.

[39] Q. Wang, M. Ihme, Regularized deconvolution method for turbulent combustion modeling, Combust. Flame 176, 125 (2017).

[40] R.S. Cant, SENGA2 User Guide, CUED/ATHERMO/TR67, September (2012).

[41] Z.M. Nikolaou, N. Swaminathan, Direct numerical simulation of complex fuel combustion with detailed chemistry: physical insight and mean reaction rate modeling, Comb. Sc. Tech. 187, 1759 (2015).

[42] Z. Nikolaou, N. Swaminathan, A 5-step reduced mechanism for combustion of CO/H2/H2O/CH4/CO2 mixtures with low hydrogen/methane and high H2O content, Combust. Flame 160, 56 (2013).

[43] Z.M. Nikolaou, N. Swaminathan, J.Y. Chen, Evaluation of a reduced mechanism for turbulent premixed combustion, Combust. Flame 161, 3085 (2014).

[44] N. Peters. Laminar flamelet concepts in turbulent combustion. 21st Symp. (Int.) on Combustion, The Combustion Institute, Pittsburgh, 1231-1250 (1986).

[45] P.A. Jansson, Deconvolution with applications in spectroscopy, New York: Academic ch. 3-4, 67-134 (1984).

[46] P. Benjamin, A quantitative evaluation of various iterative deconvolution algorithms,

IEEE 40, 558 (1991).

[47] Z.M. Nikolaou, L. Vervisch. A priori assessment of an iterative deconvolution method for LES sub-grid scale variance modelling. Flow Turb. Combust. (2018). `https://link.springer.com/article/10.1007/s10494-017-9884-0`

[48] P.H. Van Cittert, Zum Einfluss der Spaltbreite auf die Intensittverteilung in Spektralinien. II, Z. Physik, 69 298 (1931).

[49] A. Polesel, G. Ramponi, V.J. Mathews, Image enhancement via adaptive unsharp masking, 9 505 (2000).

[50] W. Layton, M. Neda, A similarity theory of approximate deconvolution models of turbulence, J. Math. Anal. Appl. 333, 416 (2007).